Atmospheric
Measurement
Techniques

Observation of tropospheric δD by IASI over western Siberia: comparison with a general circulation model

M. Pommier[1,2], J.-L. Lacour[3], C. Risi[4], F. M. Bréon[1], C. Clerbaux[2,3], P.-F. Coheur[3], K. Gribanov[5], D. Hurtmans[3], J. Jouzel[1], and V. Zakharov[5]

[1]LSCE-IPSL, UMR8212, CEA-CNRS-UVSQ, CEA Saclay, 91191, Gif-sur-Yvette, France
[2]UPMC Univ. Paris 06; Université Versailles St-Quentin; UMR8190, CNRS/INSU, LATMOS-IPSL, Paris, France
[3]Spectroscopie de l'Atmosphère, Chimie Quantique et Photophysique, Université Libre de Bruxelles (ULB), Brussels, Belgium
[4]UPMC Univ. Paris 06; UMR8539, CNRS/INSU, LMD-IPSL, Paris, France
[5]Climate and Environmental Physics Laboratory, Ural Federal University, Russia

Correspondence to: M. Pommier (matthieu.pommier@latmos.ipsl.fr)

Abstract. This study presents the joint $H_2^{16}O$ and HDO retrieval from Infrared Atmospheric Sounding Interferometer (IASI) spectra over western Siberia. IASI is an instrument on board the MetOp-A European satellite. The global coverage of the instrument and the good signal-to-noise ratio allow us to provide information on δD over this remote region. We show that IASI measurements may be used to estimate integrated δD between the surface and 3 km altitude or from 1 to 5 km depending on the thermal contrast, with observational errors lower than 4 % and 7 %, respectively. The retrieved data are compared to simulations from an isotopic general circulation model, LMDZ-iso for 2011. The satellite measurements and the model agree well and they reproduce well the seasonal and day-to-day variations for δD, presenting a good correlation (r up to 0.8 with the smoothed data in summer). The IASI-based retrievals also show the seasonal variation of the specific humidity in both altitude ranges.

1 Introduction

Siberia covers 77 % of the Russian territory but it is almost unpopulated (3 inhab km^{-2}). Siberia is important in the context of anthropogenic climate change which largely impacts this region (IPCC, 2007) mainly covered by tundra, forests and lakes. The area has undergone a sharp increase of temperatures for the last decades, which in turn has induced changes in the biogeochemical cycles and the hydrological cycle (e.g. Kane, 1997; Lapshina et al., 2001).

Water vapour is a key atmospheric compound and the dominant greenhouse gas in the Earth's atmosphere (Kiehl and Trenberth, 1997; Schmidt et al., 2010). It plays an important role in the radiative transfer (Hartmann, 2002; Soden and Held, 2006; Bony et al., 2006), the large-scale circulation (Sherwood et al., 2010), cloud formation (Luo and Rossow, 2004), precipitation (Bretherton et al., 2004) and stratospheric chemistry (Fueglistaler et al., 2009). The water cycle strongly controls various feedback mechanisms of the Earth system in response to perturbations of the energy balance of the troposphere, such as cloud and ice/snow-albedo feedbacks. The water cycle is also coupled to the surface energy budget by latent heat fluxes associated with evaporation and condensation. However, many aspects of the water cycle are still uncertain. The measurement of the isotopic ratio of water, comparing the abundance of the heavier isotopologues (principally $H_2^{18}O$, $H_2^{17}O$ and HDO) to the main isotopologue $H_2^{16}O$, can provide additional information about these processes and about the sources of water vapour.

Indeed, the chemical properties of all isotopologues are similar but their masses are different. There is a fractionation of the different isotopologues during evaporation/condensation processes due to the differences in vapour pressures and diffusivities in air.

The isotopic composition is given in per mil (‰) units using the conventional δ notation relative to the V-SMOW standard (Vienna-Standard Mean Ocean Water). This is the reference standard for water isotope ratios (Craig, 1961). Our work focuses on δD as δ^{18}O and δ^{17}O are still challenging to retrieve from remotely sensed observations. δD is expressed as

$$\delta D = 1000 \times (\frac{HDO/H_2O}{R_{VSMOW}} - 1), \tag{1}$$

where $R_{VSMOW} = 0.31152 \times 10^{-3}$. Hence δD gives an indication on the abundance of HDO relative to that of H_2O. A δD of 0 ‰ indicates that the ratio is equal to that of sea water. A value of -500 ‰ means that the ratio in the sample is only half that of the ratio in sea water, and a value of -1000 ‰ means that the sample contains no HDO.

The study of the water isotopes has been carried out for many years in various scientific fields. The analysis of ice cores has improved our understanding of past climate (e.g. Jouzel et al., 2007). The spatial and temporal analysis of stable water isotopologue distribution in precipitation across the globe has a potential to improve our understanding of the hydrological cycle (e.g. Gat, 2000). In ecology, stable water isotopologues are used to evaluate soil evaporation, plant transpiration, drought effects on vegetation and water sources for different plants (e.g. Farquhar et al., 2007). These studies highlight the importance of a detailed understanding of the mechanism of the isotopic signal in atmospheric water vapour and thus the importance of the improvement of its measurements.

In recent years the improvement in instrumental performances has made it possible to measure the water vapour isotopic signal from the measurements acquired by spaceborne instruments, with the Infrared Atmospheric Sounding Interferometer (IASI) among them. Herbin et al. (2009) first showed the possibility to detect δD with IASI and they analysed the distribution during a typhoon event over Southeast Asia. In their work, they retrieved separately HDO and H_2^{16}O, and then calculated the δD values according to Eq. (1) as done in numerous studies. Schneider and Hase (2011) performed a validation work over Tenerife and Lacour et al. (2012) presented results for the 3–6 km distribution, both presenting a δD retrieval.

Prior to IASI, the Interferometric Monitor for Greenhouse gases (IMG) (Zakharov et al., 2004; Herbin et al., 2007) and the Tropospheric Emission Spectrometer (TES) provided quasi-global distributions of δD representative of the mid-troposphere (e.g. Worden et al., 2006, 2007) whereas the SCanning Imaging Absorption spectrometer for Atmospheric CartograpHY (SCIAMACHY) instrument provided total column distributions, with sensitivity down to the boundary layer (Frankenberg et al., 2009). Both TES and SCIAMACHY distributions required significant time averaging to reach the global scale, which puts a limit on what can be expected for monitoring the short-term variability of water. The Thermal And Near infrared Sensor for carbon Observation – Fourier Transform Spectrometer (TANSO-FTS) (e.g. Boesch et al., 2013; Frankenberg et al., 2013) can also be used to derive the δD total column distribution, and the Atmospheric Chemistry Experiment – Fourier Transform Spectrometer (ACE-FTS) gave information on the δD variability in the tropical tropopause layer (Nassar et al., 2007) but, as for TES and SCIAMACHY, their global coverage is still limited compared to IASI. The TES retrieval is relatively similar to the IASI δD retrieval, using a fixed a priori as well, while the other mission provided δD data based on separated HDO and H_2^{16}O retrievals.

This work documents for the first time δD retrievals from IASI radiances over land and at high latitudes. While the methodology to retrieve spectra measured above land was already developed in Lacour et al. (2012), the present data set is interesting in that it includes cases with high thermal contrasts (ΔT) which greatly impact the sensitivity of the retrieval. Generally, high-latitude retrievals are more challenging than low- and mid-latitude retrievals, mainly due to the cold-temperature profiles of the atmosphere and the lower concentration of water vapour that affect the information content present in the measurement. To cope with that difficulty, a specific a priori covariance matrix for high-latitude retrievals was built in order to better constrain the solutions of the inverse problem.

One of the rationales for the present study is to acquire a first IASI δD data set for the high-latitude regions for comparison with model simulations, which have been suggested to have deficiencies at these high latitudes (Risi et al., 2012a). Furthermore, models also underestimate the role of the continental recycling at mid-latitudes as over Siberia (e.g. Risi et al., 2013). Thanks to the joint effort from different communities within the Russian–French WSIBISO project (http://wsibiso.ru), the new data set from IASI retrievals allows us to evaluate the performance of isotopic general circulation models (GCMs) over Siberia. This project aims to better document the water and the carbon cycle over peatlands and permafrost regions of western Siberia and their projected changes under a warming climate, focusing on isotopic studies. WSIBISO is based on a combining approach with observations (using both surface measurements and satellite data), as well as land surface and permafrost models as atmospheric models. Here we use the isotopic version of the LMDZ model, LMDZ-iso (Risi et al., 2010).

A global description of the IASI mission is given in Sect. 2. Section 3 presents the methodology used and provides a detailed characterization of the retrieved δD, under different thermal contrast conditions. The results are presented, and compared with LMDZ-iso in Sect. 4. The conclusions are presented in Sect. 5.

2 Overview of IASI observations

IASI is a nadir-viewing Fourier transform spectrometer instrument. The first model (IASI-A), was launched in October 2006. The second instrument was launched in September 2012. The wide swath of the IASI instrument provides near-global coverage twice daily with a local time of observation close to 9:30 a.m. and 9:30 p.m. IASI measures in the thermal infrared part of the spectrum, between 645 and 2760 cm^{-1}. It records radiance from the Earth's surface and the atmosphere with an apodized spectral resolution of 0.5 cm^{-1}, spectrally sampled at 0.25 cm^{-1}. It has a low noise of 0.1–0.4 K for a reference blackbody at 280 K (Hilton et al., 2012), with the lower noise values in the range used for δD retrievals (e.g. Lacour et al., 2012). The IASI atmospheric view is composed of 2×2 circular pixels each with a ground footprint of 12 km diameter at nadir and it has an across-track scan with a swath width of 2200 km. Owing to its large swath IASI provides a large number of observations per day even over small areas; this is illustrated for instance in Fig. 1, which shows a sampling around the city of Yekaterinburg for one day. This area is referred to hereafter as YEK.

$H_2^{16}O$, $H_2^{18}O$ and HDO are the three main isotopologues of water having large absorption bands in the thermal infrared region. Spectral signatures of these species are well detected by IASI. However, as explained by Herbin et al. (2009), a meaningful retrieval of the $H_2^{18}O / H_2^{16}O$ ratio is very challenging as its variation in the atmosphere is small. This is not the case for the HDO / $H_2^{16}O$ ratio for which IASI was shown earlier to provide results of sufficient accuracy. In the following, we therefore focus on the retrievals of HDO and $H_2^{16}O$ in order to study the δD variations. The selected spectral ranges are 1195–1223.5 cm^{-1} and 1251.25–1253 cm^{-1} (Fig. 2), avoiding the major interferences of CH_4 and N_2O. In order to simplify the notations, the main isotopologue $H_2^{16}O$ will be named hereafter as H_2O.

As there are numerous IASI data (more than one million observations per day) and as the retrieval procedure for δD currently relies on a line-by-line approach that is computationally expensive, we have chosen to process only one pixel out of four. Furthermore, only spectra with a cloud fraction (see IASI Level 2 Product Guide, 2008) below or equal to 10 % are considered and the few unrealistic positive retrieved δD values are filtered out. Overall this restricts the data set to 9 % of the observations (15 234 out of 175 528) over the Siberia area for the year 2011. Despite these strict criteria and as shown in Fig. 1 for 1 day, the YEK area is still well covered by IASI.

3 Retrieval methodology summary

The methodology used to retrieve HDO / H_2O ratios from IASI radiances is overall similar to that presented in Lacour et al. (2012), which itself was stimulated by the earlier developments on the retrieval of δD presented by Schneider et al. (2006) and Worden et al. (2006). As compared to Lacour et al. (2012), the retrieval settings have been optimized for the specificity of the high-latitude region analysed here. We also apply the methodology developed by Schneider et al. (2012) to ensure that we analyse H_2O and δD products representative of the same air mass and that the cross-dependence between them is minimized. Hereafter, we briefly introduce the general concepts of the optimal estimation method (OEM), and we describe the new information a priori and the new retrieval characterization.

3.1 General aspects of the retrieval methodology

In this study we use for the retrieval the line-by-line radiative transfer code "Atmosphit" developed at Université Libre de Bruxelles to retrieve HDO/H_2O ratios from IASI spectra, using the HITRAN database for spectroscopic parameters (Rothman et al., 2009). It relies on the OEM described by Rodgers (2000) and has been adapted to perform the retrieval on a natural logarithmic scale and to optimally retrieve HDO / H_2O ratios (Lacour et al., 2012).

A forward model $\mathbf{F}$ needs to describe the physics of the measurement. An atmospheric state vector can be related analytically to $\mathbf{F}$ by

$$y = \mathbf{F}(x, b) + \varepsilon = \mathbf{K}(x - x_a) + \boldsymbol{\varepsilon}, \tag{2}$$

where y corresponds to the measurement vector (IASI radiances), $\boldsymbol{\varepsilon}$ is the instrumental noise, x the state vector that contains the parameters to be retrieved, and b the vector containing all other model parameters impacting the measurement (e.g. emissivity, temperature profiles, etc.). Equation (2) highlights the linear approximation of relationship between x, the a priori vector x_a, weighted by the weighting function matrix $\mathbf{K}$ (also named Jacobians matrix) and ε. The Jacobians matrix $\mathbf{K}$ is expressed as

$$\mathbf{K} = \frac{\partial \mathbf{F}(x)}{\partial x}. \tag{3}$$

As explained in Rodgers (2000), the solution is found by

$$\hat{x} = x_a + (\mathbf{K}^T \mathbf{S}_\epsilon^{-1} \mathbf{K} + \mathbf{S}_a^{-1})^{-1} \mathbf{K}^T \mathbf{S}_\epsilon^{-1} (y - \mathbf{K} x_a), \tag{4}$$

where $\mathbf{S}_\epsilon$ is the measurement error covariance, and $\mathbf{S}_a$ is the a priori covariance matrix. Equation (4) shows that the retrieved profile $\hat{x}$ combines the information from the measurement and the a priori.

The OEM solution can be found by iteratively applying

$$x_{i+1} = x_i + (\mathbf{K}_i^T \mathbf{S}_\epsilon^{-1} \mathbf{K}_i + \mathbf{S}_a^{-1})^{-1}$$
$$\mathbf{K}_i^T \mathbf{S}_\epsilon^{-1} [y - \mathbf{F}(x_i) + \mathbf{K}_i (x_i - x_a)]. \tag{5}$$

The iteration starts with the initialization of the a priori conditions (x_a and $\mathbf{S}_a$) and terminates when convergence is achieved.
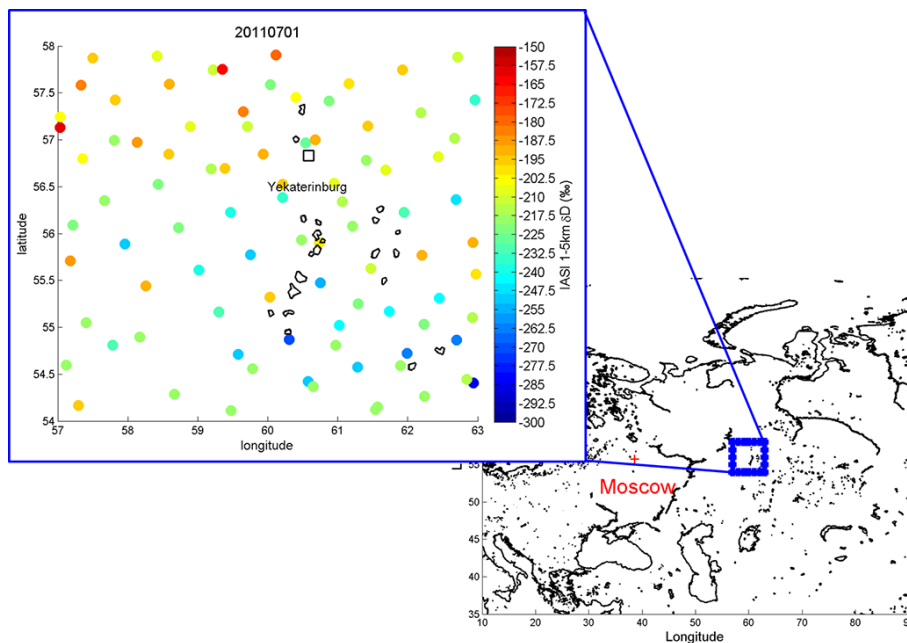
Figure 1. IASI cloud-free observation of 1–5 km δD (in ‰) over the Yekaterinburg area (YEK) on 1 July 2011; only one pixel out of four is processed and shown. Each circle represents the observation at the location of the centre of each pixel. The city is marked with the square.

3.2 Particularity of the δD retrieval: the HDO / H$_2$O correlated approach

The retrieval of water isotopologues requires applicability over a wide dynamical range (because of the high variability of water) and at the same time high precision to capture the small isotopic variations. The HDO / H$_2$O correlated approach makes it possible to constrain the retrieval taking into account the probability density function of the ln(HDO)–ln(H$_2$O) distribution which is more stable than H$_2$O variability (Schneider et al., 2006).

Performing the retrieval on a natural logarithm scale and including the correlation between ln(HDO) and ln(H$_2$O) helps to constrain the joint HDO / H$_2$O retrieval to a physically meaningful solution. This method also has the large advantage of minimizing the error on the δD profile (e.g. Schneider et al., 2006) as demonstrated for example by Worden et al. (2006, 2007, 2012) on TES measurements, on IASI measurements by Schneider and Hase (2011) and Lacour et al. (2012), or for ground-based measurements by Schneider et al. (2006, 2010, 2012).

Compared to the IASI/MUSICA retrieval approach (Schneider and Hase, 2011; Wiegele et al., 2014), a smaller spectral range is used to lower contamination with interfering species and the temperature profiles are not adjusted. Instead, we use the EUMETSAT L2 retrieved temperature profile for each IASI field of view (Lacour et al., 2012).
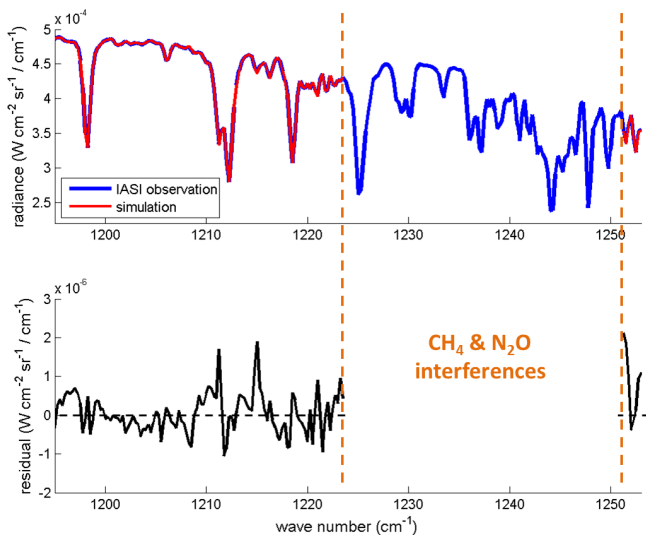

Figure 2. Upper panel: IASI observed spectra (blue curve), the calculated spectra (red curve) in radiance units for August 2011. Bottom panel: the corresponding residual is plotted in black, with an rms of 1.05×10^{-6} W cm^{-2} sr^{-1}/cm^{-1}. Note the factor 100 between the residual and the radiance. The gap on the residual highlights the part where the retrieval is not performed, avoiding major CH$_4$ and N$_2$O interferences.

3.3 A priori information

We use a single a priori profile developed specifically for western Siberia (Fig. 3) for all conditions (season). The use of a single a priori allows for a simpler analysis of the latitudinal, longitudinal and seasonal distribution of HDO, H_2O and thus of δD, as there is no change in the a priori.

The a priori matrix, which corresponds to a measure of the knowledge of the state vector prior to the measurement, is provided by the covariance matrix $\mathbf{S}_a$. The choice of the a priori is a tricky task in order to correctly pose the problem. The covariance matrix describes to which extent parameters co-vary, for an ensemble of vectors. The diagonal elements of these matrices correspond to the variance of each parameter. Our state vector is based on correlations between $\ln(H_2O)$ and $\ln(HDO)$ profiles. Within one profile, different altitude levels are correlated and there are also strong correlations between $\ln(H_2O)$ and $\ln(HDO)$. These correlations can be captured in a total covariance matrix $\mathbf{S}_a$, which can naturally be grouped into four sub-blocks as

$$\mathbf{S}_a = \begin{bmatrix} \mathbf{S}_{a\,hh} & \mathbf{S}_{a\,dh} \\ \mathbf{S}_{a\,hd} & \mathbf{S}_{a\,dd} \end{bmatrix}, \tag{6}$$

where the two sub-blocks $\mathbf{S}_{a\,hh}$ and $\mathbf{S}_{a\,dd}$ are the covariance matrices of the $\ln(H_2O)$ and $\ln(HDO)$, respectively. The matrices $\mathbf{S}_{a\,hd}$ and $\mathbf{S}_{a\,dh}$ contain the correlations between $\ln(H_2O)$ and $\ln(HDO)$. The a priori information was built from outputs from the LMDZ-iso model (Risi et al., 2010).

As can be seen in Fig. 3c and d, the δD a priori variability reaches up to 18 % (80 ‰) and varies from 8 to 14 % (15–50 ‰) from the surface to 5 km. The H_2O variability introduced in our retrieval is about 90 % (up to 1.5 g kg^{-1}) from the surface to the free troposphere. In comparison with IASI retrievals used in Lacour et al. (2012), our variability is more constrained.

3.4 The measurement noise

The measurement variance–covariance matrix includes the instrumental noise. Hereafter, it is assumed to be diagonal, $\mathbf{S}_\epsilon = \sigma_\epsilon^2\,\mathbf{I}$, where σ_ϵ is a constraint representing the noise equivalent spectral radiance and estimated at 5×10^{-9} W (cm^2 sr cm^{-1})$^{-1}$. This value is slightly higher than the IASI spectral noise estimated in the selected spectral range, for a temperature at 280 K ($\sim 3.5 \times 10^{-9}$ W (cm^2 sr cm^{-1})$^{-1}$) (Clerbaux et al., 2009). Note also interestingly that the value of σ_ϵ used here is smaller than the one used in Lacour et al. (2012) (8×10^{-9} W (cm^2 sr cm^{-1})$^{-1}$). This reflects the better spectral fits obtained with IASI in regions with lower humidity, such as those analysed here. For the sake of illustration, Fig. 2 gives an example of a spectral fit in the selected windows. More generally, the fits are characterized by a yearly root mean square (rms) on average of the residuals of 5.5×10^{-9} W (cm^2 sr cm^{-1})$^{-1}$, with better rms obtained in winter and in autumn than in the summer since

humid scenes give saturated spectral features that are more difficult to adjust.

3.5 Sensitivity of the measurement to the different isotopologues

The Jacobians are the partial derivative of the radiance with respect to the concentration for each isotopologue and integrated over each retrieval layer (1 km). The Jacobians show how the radiance would change to a fractional change in the concentration as illustrated in Fig. 4.

In Fig. 4, the Jacobians of H_2O and HDO are plotted as a function of the altitude in the selected spectral window. It is worth noting that the sensitivity of the measurement varies as a function of thermal contrast, which is the difference between the surface temperature and the temperature of the first layer of the atmosphere. In Siberia, the yearly absolute mean thermal contrast $|\Delta T|$ is 5 K, depending on the time of the year. Note for example that the mean ΔT in January is -8 K and in July $+4$ K.

This plot illustrates the impact of the thermal contrast with two cases, one with a low (Fig. 4a) and one with a high (Fig. 4b) absolute value of the thermal contrast (for July 2011). The thresholds of 4 K and 8 K used hereafter represent the median and the 75th percentile of the $|\Delta T|$ distribution on 2011 over YEK, respectively. The altitudes of maximum sensitivity are different for each isotopologue. This maximum is highlighted by the dark blue colour showing the most negative derivatives corresponding to the largest derivatives.

With a large thermal contrast, the isotopologues are detectable closer to the surface. With a low thermal contrast, the maximum sensitivity is achieved between 1 and 6 km for H_2O, while it ranges from 1 to 5 km for HDO.

3.6 Retrieval characterization

3.6.1 Vertical sensitivity of the retrieval

The averaging kernel (AK) matrix is composed of elements that are the derivatives of the estimated state $\hat{\boldsymbol{x}}$ with respect to the state vector $\boldsymbol{x}$:

$$\mathbf{A} = \frac{\partial \hat{\boldsymbol{x}}}{\partial \boldsymbol{x}} = \mathbf{GK}. \tag{7}$$

$\mathbf{G}$ is the gain matrix whose rows are the derivatives of the retrieved state with respect to the spectral points and it is defined by

$$\mathbf{G} = \frac{\partial \hat{\boldsymbol{x}}}{\partial y} = (\mathbf{K}^T \mathbf{S}_\epsilon^{-1} \mathbf{K} + \mathbf{S}_a^{-1})^{-1} \mathbf{K}^T \mathbf{S}_\epsilon^{-1}. \tag{8}$$

$\boldsymbol{x}$ and $\hat{\boldsymbol{x}}$ are expressed in logarithmic space and thus the AK noted $\mathbf{A}$ is unitless. This AK can be written as

$$\mathbf{A} = (\mathbf{K}^T \mathbf{S}_\epsilon^{-1} \mathbf{K} + \mathbf{S}_a^{-1})^{-1} (\mathbf{K}^T \mathbf{S}_\epsilon^{-1} \mathbf{K}). \tag{9}$$
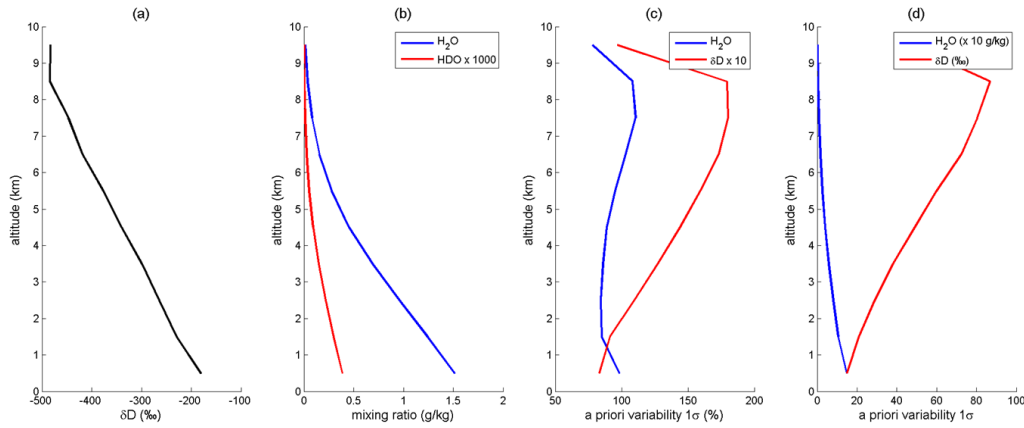
Figure 3. A priori profiles used in the retrieval for δD in ‰ **(a)**, for H$_2$O and HDO (in g kg^{-1}), plotted in blue and red curves, respectively **(b)**. The a priori variability 1σ for H$_2$O and δD are expressed in % **(c)** and in their respective unit – in g kg^{-1} for H$_2$O and in ‰ for δD **(d)**.

Thus Eq. (5) becomes

$$\hat{x} = x_a - Ax_a + (K^T S_\epsilon^{-1} K + S_a^{-1})^{-1} K^T S_\epsilon^{-1} y. \qquad (10)$$

AKs are commonly used to evaluate the vertical sensitivity of the retrieval with the peak indicating the altitude of maximum sensitivity and the full width at half maximum, the vertical resolution. The degree of freedom of the signal (DFS), corresponding to the trace of the AK, expresses the quantity of independent vertical information in the retrieval. In the case of the HDO / H$_2$O correlated retrieval, the averaging kernels corresponding to the state vector x are defined as follows:

$$A = \begin{bmatrix} A_{hh} & A_{dh} \\ A_{hd} & A_{dd} \end{bmatrix}, \qquad (11)$$

with A_{hh}, A_{dd}, expressing the sensitivity of the estimate state to the true state for ln(H$_2$O), ln(HDO) respectively; and A_{hd} and A_{dh}, the real ln(HDO) affecting the retrieved ln(H$_2$O) and real ln(H$_2$O) affecting the retrieved ln(HDO). An illustration of the AKs is given in Fig. 5a for a $|\Delta T| < 4$ K and in Fig. 5b for $|\Delta T| > 8$ K.

With $|\Delta T| < 4$ K, the vertical sensitivity ranges between 1 and 5 km for HDO (Fig. 5a, bottom right) while for H$_2$O, it is more homogeneous on the vertical (Fig. 5a, top left) with clear surface sensitivity. HDO is generally the limiting component (with respect to the sensitivity) to the HDO / H$_2$O retrieval. HDO AKs are often used as a proxy of δD AKs. As described before, the retrieval presents a larger sensitivity close to the surface with a higher thermal contrast (Fig. 5b). For the year 2011, over YEK, the averaged AKs present a higher sensitivity in the mid-troposphere even if we have to be aware that the thermal contrast highly impacts the vertical representativity of δD.

Schneider et al. (2012) suggested an optimal use of humidity and δD retrievals by a posteriori correction. Their method makes it possible to transform the {ln(H$_2$O), ln(HDO)}-state

onto a {humidity, δD}-proxy state, useful for the common study of both parameters in a same air mass. The advantage of their posteriori processing is that it determines a proxy-δD AK reducing the cross-dependence of both isotopologues. The final result of this procedure named A'' (Schneider et al., 2012) is shown in Fig. 6 for each compound (A''_{hh}, A''_{dd}, A''_{hd}, A''_{dh}) and for both thermal conditions, low (Fig. 6a) and high (Fig. 6b) $|\Delta T|$. As explained in Schneider et al. (2012), the kernels A''_{hd}, A''_{dh} are scaled by a factor of 0.08 and 12.5, respectively. With their technique, the humidity and δD present the same vertical resolution, and cross-dependence between δD and H$_2$O is minimized. Even if the DFS is limited, this shows that IASI resolves the same air mass for both isotopologues. This transformation of the AKs sheds further light on the dependency of the retrieval on the local thermal contrast, with the A'' characterized by very different shapes. For low thermal contrast (Fig. 6a), the surface sensitivity for δD is vanishing and the information reduces to the integrated [1–5 km] column; the DFS is typically 0.7. When the thermal contrast is larger (Fig. 6b), the AK peaks at the surface and decreases rapidly, reaching very small values already at 4 km; the DFS is then slightly larger, around 0.8. Note, however, that the number of observations with large values of $|\Delta T|$ is not so frequent so that on the yearly average, the most representative sensitivity is that depicted in Fig. 6a.

3.6.2 Error characterization

The error on the retrieval can be calculated as the difference between the retrieved state and the true state. Thus from Eqs. (8) and (10) it is expressed as

$$\hat{x} - x = (A - I)(x - x_a) + G\epsilon + GK(x - x_a). \qquad (12)$$

The total error is thus composed of three terms: $(A - I)$ $(x - x_a)$ represents the smoothing error, which accounts for the vertical sensitivity of the measurements to the retrieved
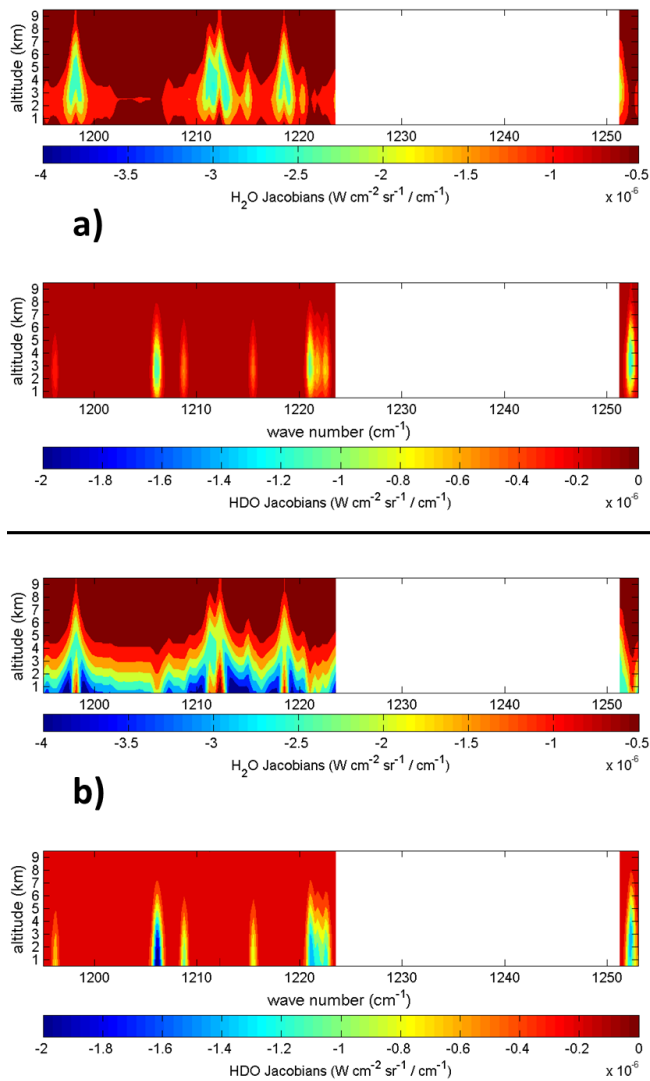
Figure 4. Monthly Jacobian means of H_2O (upper panel) and HDO (bottom panel) as a function of altitude and wave number for July 2011 with a low ($< 4\,K$) **(a)** and a large ($> 8\,K$) **(b)** absolute value of thermal contrast. The smallest derivative values indicate the maximum sensitivities (dark blue). As in Fig. 2, the gap highlights the part where the retrieval is not performed, avoiding major CH_4 and N_2O interferences.

Figure 5. Mean AKs (**A**) with a $|\Delta T| < 4\,K$ **(a)** and with a $|\Delta T| > 8\,K$ **(b)** in 2011. See text for the definition of $\mathbf{A_{hh}}$, $\mathbf{A_{dd}}$, $\mathbf{A_{hd}}$ and $\mathbf{A_{dh}}$ and for the explanation of both panels. The coloured curves and dots aim to help the reader to follow the variability of each AK with altitude.

profile; the second term $\mathbf{G}\boldsymbol{\epsilon}$ is the measurement error, associated with the spectral noise; and $\mathbf{G}\,\mathbf{K}\,(\boldsymbol{x} - \boldsymbol{x}_a)$ is the model parameter error representing the imperfect knowledge of the model parameters as temperature, water line list of spectroscopic parameters or surface emissivity for example.

Their covariance matrices are respectively given by

$$\mathbf{S}_{\text{smoothing}} = (\mathbf{A} - \mathbf{I})\mathbf{S}_a(\mathbf{A} - \mathbf{I})^T \tag{13}$$

$$\mathbf{S}_{\text{measurement}} = \mathbf{G}\mathbf{S}_\epsilon \mathbf{G}^T \tag{14}$$

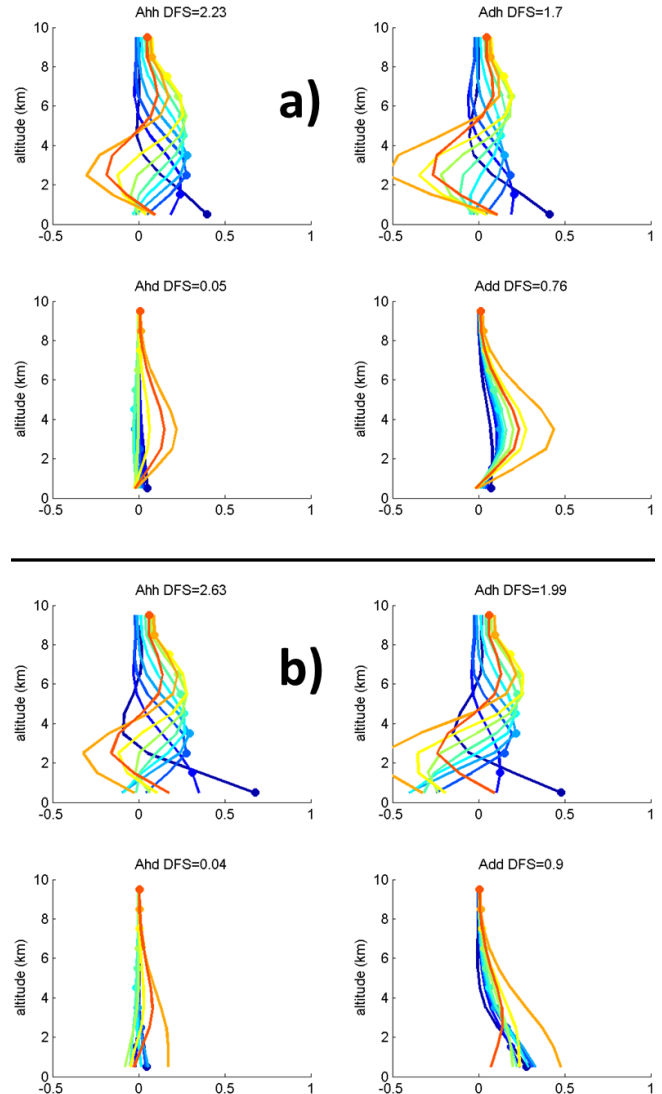$$\mathbf{S}_{\text{mod. param.}} = \mathbf{G}\mathbf{K}_b \mathbf{S}_b (\mathbf{G}\mathbf{K}_b)^T \tag{15}$$

with $\mathbf{S}_b$ representing uncertainty on the forward model parameters and $\mathbf{K}_b$ the sensitivity of the forward model to the forward parameters ($= \frac{\partial \mathbf{F}}{\partial b}$). In Eq. (13), the covariance matrix of a real ensemble of states is generally approximated by the a priori covariance matrix $\mathbf{S}_a$. Equation (13) explicitly includes a vertical sensitivity through the $\mathbf{A}$ matrix, and it is obvious that the smoothing error decreases when AKs are close to one and/or if the variability in $\mathbf{S}_a$ is small.

Following the technique described by Schneider et al. (2012), we can determine directly the δD errors (see their Eqs. 16 to 19; we also apply the operators $\mathbf{P}$ of their Eq. 6 and $\mathbf{C}$ of their Eq. 14 on $\mathbf{S}_{\text{measurement}}$ as: $\mathbf{C}\,\mathbf{P}\mathbf{S}_{\text{measurement}}\,\mathbf{P}^T \mathbf{C}^T$). The error budget for H_2O and δD is presented for both a low (Fig. 7a) and a high (Fig. 7b) thermal contrast.
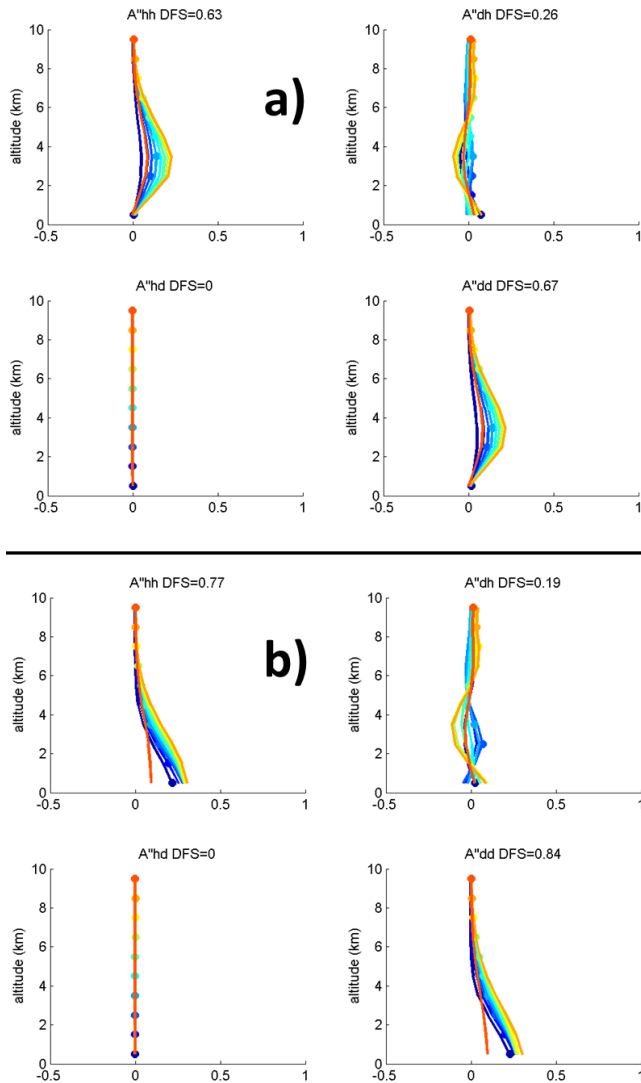
Figure 6. As Fig. 5, for $\mathbf{A''}$, representing the { humidity, proxy-δD } state.

Figure 7. Mean error profiles (quadratic sum of covariance) for 2011 with $|\Delta T| < 4\,\text{K}$ **(a)** and $|\Delta T| > 8\,\text{K}$ **(b)** for air temperature, measurement noise, smoothing, and the total observational ($\sqrt{\text{temperature}^2 + \text{measurement noise}^2}$), for H_2O (left) and δD (right) for the { humidity, proxy-δD } state.

Reducing the vertical sensitivity of H_2O to the δD one gives a higher smoothing error for H_2O than considering the full sensitivity of H_2O ($\mathbf{A}$). This smoothing error goes up to 56 % for H_2O and 5 % for δD close to the surface with a high $|\Delta T|$. In the mid-troposphere, with a low $|\Delta T|$, the smoothing error reaches 56 % for H_2O and 6 % for δD. Moreover, the uncertainties on the temperature profile are the main sources on the total observational errors ([1–5 km]: < 14 % for H_2O and < 7 % for δD with a low $|\Delta T|$, [0–3 km]: ≤7 % for H_2O and ≤ 3 % for δD with a high $|\Delta T|$) (Fig. 7). To better evaluate the error due to uncertainties in the temperature, we use the forward simulation approach as performed in Lacour et al. (2012) since we do not retrieve the temperature profile. We modify the temperature profiles of 0.5 % at each level. This perturbation is larger than the uncertainties found in Pougatchev et al. (2009). Differences between the origi-
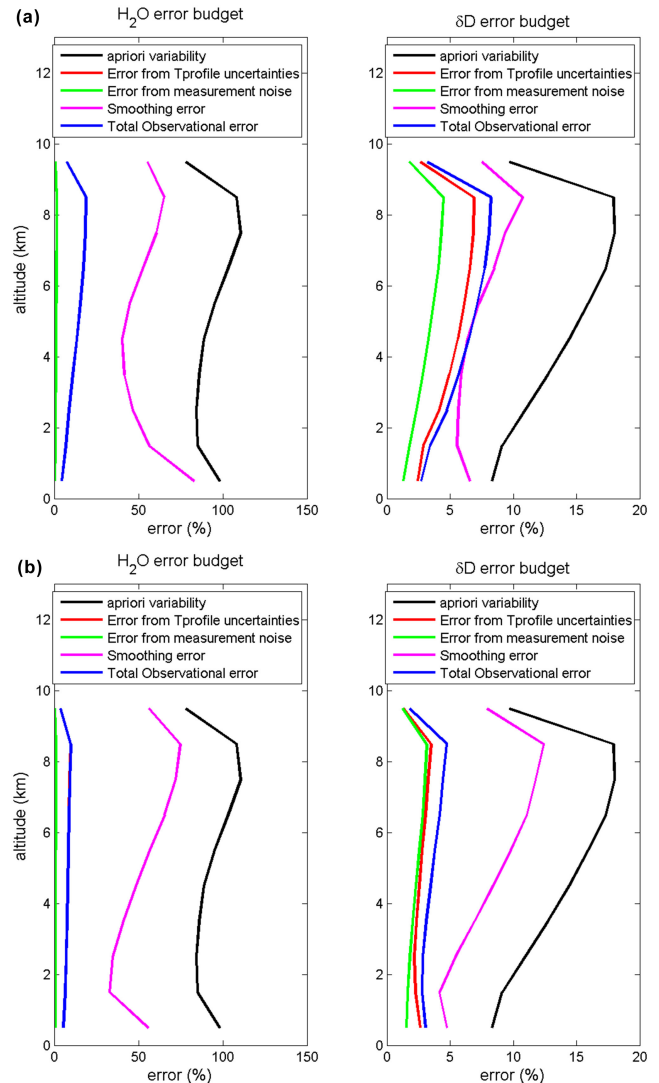
nal and these new retrieved profiles allow us to estimate the error from the temperature profile. With $|\Delta T| < 4\,\text{K}$, the difference between both profiles is below 48 ‰ in the [1–5 km] altitude range. With $|\Delta T| > 8\,\text{K}$, this difference is lower than 15 ‰ between 0 and 3 km.

4 Observations of the seasonal variability: comparison with a GCM

4.1 The isotopic general circulation model: LMDZ-iso

The resolution of the GCM LMDZ4 (Hourdin et al., 2006) used here is 2.5° in latitude, 3.75° in longitude and 19 vertical levels from the surface up to 3 hPa (~ 35 km). The physical package includes the Emanuel convective scheme (Emanuel, 1991; Emanuel and Zivkovic-Rothman, 1999) and a statistical cloud scheme (Bony and Emanuel, 2001). Water vapour and condensate are advected using a second-order monotonic finite-volume advection scheme (Van Leer, 1977; Hourdin and Armengaud, 1999).

Water isotopic species ($H_2^{16}O$, $H_2^{18}O$ and HDO) are transported and mixed passively by the large-scale advection and various air mass fluxes. There is no fractionation during the evapotranspiration over land, as done in most other GCMs due to the simplicity of the land surface parameterization (e.g. Hoffmann et al., 1998; Lee et al., 2007). The representation of the re-evaporation and diffusive exchanges as the rain falls is significantly different compared to other GCMs (e.g. Hoffmann et al., 1998). The relative proportion of evaporative enrichment and diffusive equilibration is calculated depending on relative humidity. LMDZ-iso also takes into account the evolution of the compositions of both the rain and the surrounding vapour as the rain drops re-evaporate. The isotopic version of the LMDZ GCM is described in more detail by Risi et al. (2010).

4.2 Seasonal variability of the tropospheric water

In order to compare the satellite retrievals to the simulation values with a consistent vertical sensitivity, it is necessary to convolve the model profiles with the IASI AKs. Based on study by Schneider et al. (2012), the smoothed profiles of water mixing ratios ($q_{smoothed}$) from the model are obtained as

$$q_{smoothed} = \exp\big[\mathbf{A}''_{hh} \times \ln(q_{model}) + (\mathbf{I} - \mathbf{A}''_{hh}) \times \ln(q_{apriori})\big], \quad (16)$$

where q_{model} is the water mixing ratio from LMDZ-iso, $\mathbf{I}$ the identity matrix and $q_{apriori}$ the IASI a priori water mixing ratio. The real ratio $R = $ HDO / H_2O as seen with the sensitivity of our retrieval is

$$R_{smoothed} = \exp\big[\ln(R_{apriori}) + \mathbf{A}''_{dd} \times (\ln(R_{model}/R_{apriori}))\big]. \quad (17)$$

The terms $\mathbf{A}''_{hd}$ and $\mathbf{A}''_{dh}$ are not used since they can be seen as errors. Their use would introduce additional errors on the comparison with the model. Figure 8 shows the IASI and LMDZ-iso daily means over YEK area presented in Fig. 1, using the Schneider et al. (2012) method. The panels show the seasonal variation for the specific humidity and for the
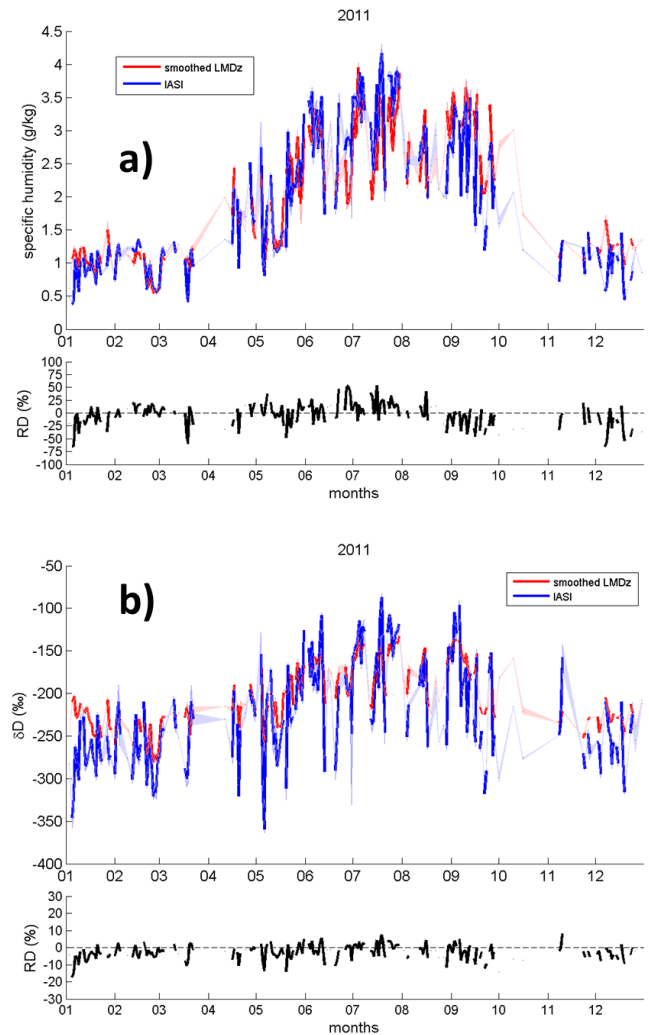

Figure 8. Daily [0–3 km] specific humidity (a) and δD (b) means by IASI (blue curve) and smoothed LMDZ-iso (red curve) for 2011 with a $|\Delta T| > 8$ K. The shade contour represents the standard deviation. The relative difference is calculated as: ((IASI-LMDZ-iso)/LMDZ-iso) $\times$ 100 %. For the RD$_{\delta D}$ calculation, δD is normalized by δD + 1000.

δD, in 2011, between 0 and 3 km altitude for a high thermal contrast. Figure 9 shows the same time series in the free troposphere, with a low thermal contrast. A relative difference (RD) is calculated for both quantities making it possible to obtain a common parameter to compare simultaneously their variation. For the RD$_{\delta D}$ calculation, each δD is normalized by δD+1000. A good agreement is found for both H_2O and δD even if higher differences are observed in winter for both altitude ranges.

Table 1. Annual mean for the error on the mean for δD and H_2O and both altitude ranges (0–3 km and 1–5 km). The error is calculated as: $\sqrt{(\mathrm{Err}T^2 + \mathrm{Err\ Meas\ noise}^2)/N}$.

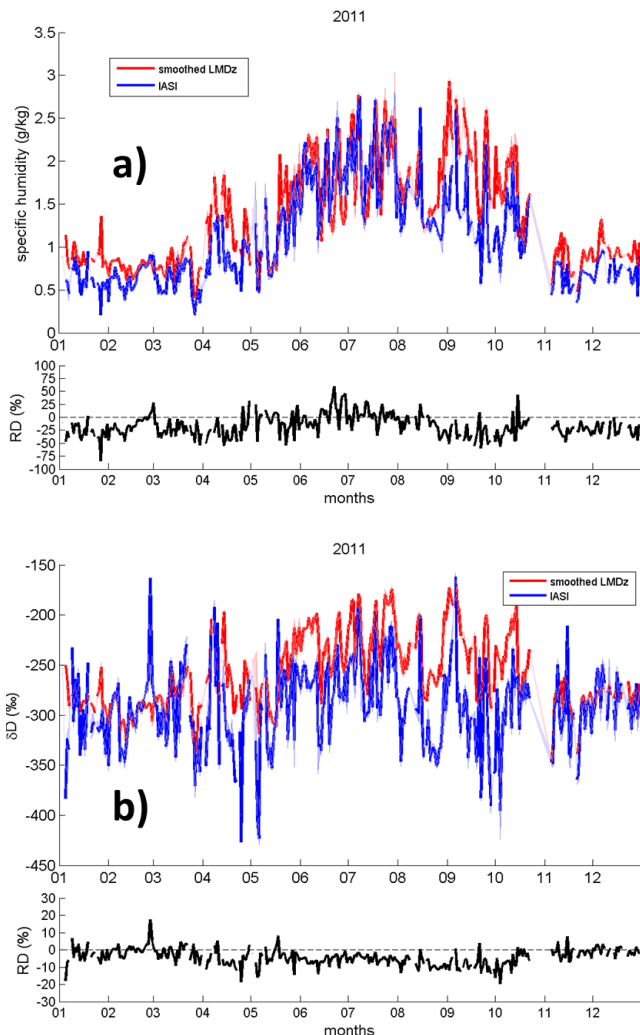|	δD (0–3 km)	δD (1–5 km)	H_2O (0–3 km)	H_2O (1–5 km)
Error on the mean (%)	2.3	3.0	3.3	5.7

Figure 9. As Fig. 8, for [1–5 km] with a $|\Delta T| < 4$ K.

4.2.1 Variability in the lower troposphere (0–3 km layer, Fig. 8)

In spite of these biases, reaching a larger RD of -65% for H_2O in the lower troposphere on 7 December (Fig. 8a), the model agrees well with the retrieval of δD from IASI ($RD_{\delta D} = -0.6\%$ on this date) (Fig. 8b). A systematic δD underestimation by IASI is however observed (mean annual $RD_{\delta D} = -2.9\%$, corresponding to a mean difference of $-22.8\permil$). The higher RD for δD (-17.2%) is reached on

5 January for 0–3 km. This corresponds to a RD for H_2O of -64.3%.

4.2.2 Variability in the free troposphere (1–5 km layer, Fig. 9)

The same trend is observed as at lower altitudes. For the humidity, a RD of -84.4% in the [1–5 km] range is reached on 27 January (Fig. 9a) but the model still agrees well with the retrieval of δD from IASI ($RD_{\delta D} = -7.9\%$ on this day) (Fig. 9b). The δD underestimation by IASI is slightly higher than in the lower troposphere, with an annual mean of -4.3% for [1–5 km], corresponding to a mean difference of $-32.6\permil$. The higher RD for δD is reached on 4 October with a value of 19.7 % (difference of $147.9\permil$), corresponding to a RD for H_2O of -56.2%.

4.2.3 Error on the mean

The error on the mean is also calculated for H_2O and δD at both altitude ranges. This error is defined as the square root of the sum of squared error covariances (temperature and measurement noise) divided by the number of samples. The values are summarized in Table 1 and are lower than the mean annual RDs. This shows that the RDs are representative of a real difference between the values from IASI and from LMDZ-iso.

4.2.4 Comparison with other measurements

The seasonal variation is relatively well captured by IASI in comparison with the LMDZ-iso modelled values for both H_2O and δD. This is a different finding compared to conclusions from Risi et al. (2012b) and references therein. They highlighted the underestimation of the δD seasonal cycles by GCMs in mid- and high latitudes.

LMDZ-iso also presents a bias on δD at mid- and high latitudes with other atmospheric sounders such as TES or TANSO-FTS (Risi et al., 2012a, 2013). The model underestimates the latitudinal gradient compared to these sounders (Risi et al., 2012a). There is an overestimation of δD by TANSO-FTS in summer, while this bias was less pronounced with TES. Nevertheless, the absolute δD values between both instruments are not directly comparable due to the lack of absolute validation. As suggested by Risi et al. (2013), the difference of sensitivity between all these instruments calls for the performance of more cross-validation exercises, not only on the mean δD but also on its variation.
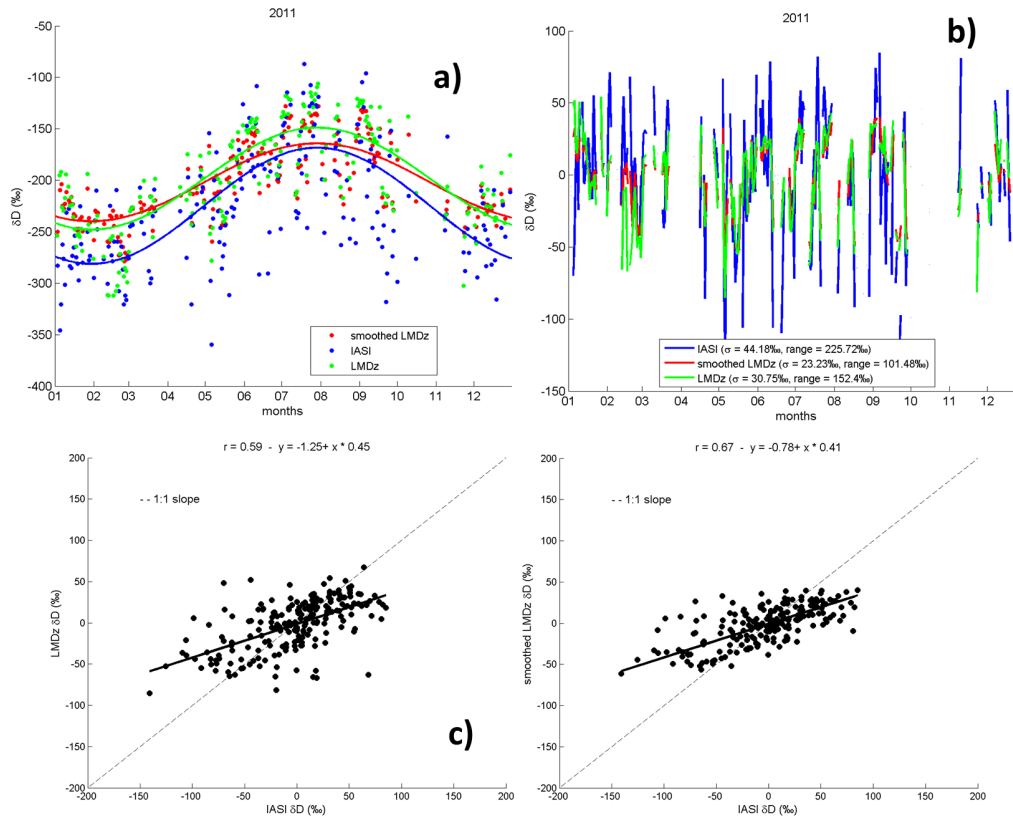
Figure 10. (a) Daily [0–3 km] δD means for IASI (blue), smoothed LMDZ-iso (red) and LMDZ-iso (green) with their seasonal trend (curve) in 2011 with a $|\Delta T| > 8$ K. This seasonal fit is defined as: $\delta D = \bar{\delta D} + SD(\delta D) \times \cos\left(\frac{2\pi}{360} \times (\text{day} - 210)\right)$. **(b)** δD deseasonalized time series obtained by subtracting daily means time series by the seasonal fit. **(c)** Scatter plot between the deseasonalized daily mean data (left: LMDZ-iso vs. IASI, right: smoothed LMDZ-iso vs. IASI). The dashed line corresponds to the theoretical 1 : 1 slope and the black line corresponds to the linear regression.

4.3 Day-to-day variability

Section 4.2 shows the IASI performance to detect the seasonal cycle, both for δD and the specific humidity. On the time series shown in Figs. 8 and 9, a large fraction of the variability results from the seasonal cycle. To analyse whether the satellite data and the model agree on the synoptic variability, it is necessary to remove this cycle. We model the cycle as a cosine function that is fitted against the data. The synoptic variations are then derived from the original estimates by subtracting the seasonal cycle. The process and results are illustrated in Fig. 10 in lower altitudes and in Fig. 11 in the free troposphere. Figures 10a and 11a show the seasonal fit. Figures 10b and 11b show the δD deseasonalized cycle obtained for IASI, smoothed LMDZ-iso (convolved with the IASI AKs) and LMDZ-iso.

In the 0–3 km altitude range, the variability obtained by the smoothed LMDZ values is underestimated by 2 compared to IASI (Fig. 10b) but higher correlation is observed (Fig. 10c). This correlation is higher with the smoothed LMDZ distribution ($r \sim 0.7$). The daily variability simulated by LMDZ in the 1–5 km range is similar to that observed by IASI

Table 2. Correlation coefficients between the deseasonalized smoothed LMDZ and IASI δD, and between the deseasonalized LMDZ and IASI δD for four seasons and both altitude ranges (0–3 km and 1–5 km).

	DJF	MAM	JJA	SON
r 0–3 km (smoothed)	0.42	0.71	0.8	0.65
r 0–3 km	0.23	0.72	0.84	0.58
r 1–5 km (smoothed)	0.19	0.66	0.8	0.46
r 1–5 km	0.06	0.67	0.78	0.53

(Fig. 11b), in terms of both standard deviation and range. However, convolving with the AKs reduces the variability, so the smoothed LMDZ actually underestimates the daily variability compared to IASI. Figure 11c shows the correlations between these daily average values, with a good agreement ($r \sim 0.6$ in both cases). For both altitude ranges, the correlation is higher in summer (JJA) ($r \sim 0.8$) (Table 2).
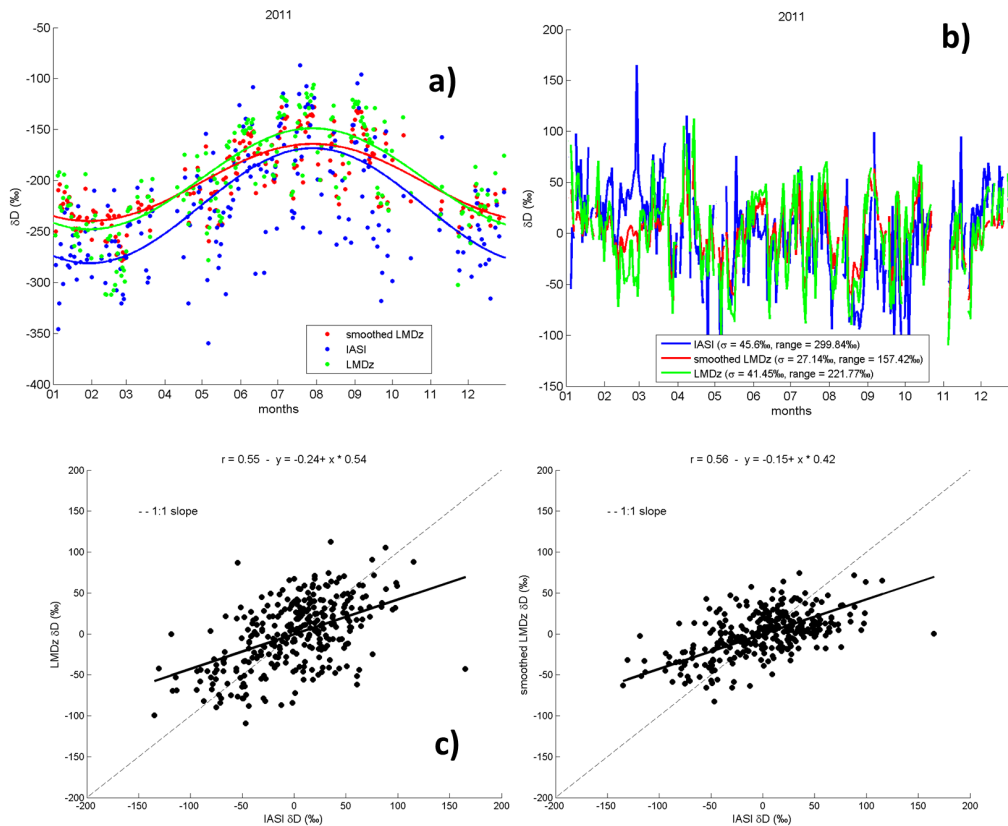
Figure 11. As Fig. 10, for [1–5 km] with a $|\Delta T| < 4$ K.

This shows that LMDZ-iso and IASI are also able to capture well the δD day-to-day variability and mostly in lower altitudes, confirming for the higher latitude what was shown earlier in tropical and subtropical regions (Lacour et al., 2012). The fact that two time series (LMDZ GCM and remotely sensed data) show a significant correlation provides some support to both of them even if the variability is underestimated with the smoothed values from the model. It demonstrates that the short-term variability does not result from random noise but is linked to true atmospheric processes.

4.4 Effect of thermal contrast on retrieved seasonal variations of the isotopic composition

As the IASI retrievals provide a good representation of the day-to-day variability, in agreement with the simulation from LMDZ-iso, and they can be used to describe the isotopic composition in the air mass over Siberia. For this, we plot the δD values as a function of the specific humidity.

As described in Sect. 3.6, the thermal contrast impacts on the vertical information provided by IASI. In our case, IASI is more sensitive close to the surface with a high thermal contrast, which occurs mainly in winter, and in the free troposphere with a low thermal contrast. Figure 12 shows

the integrated δD and H_2O between 0 and 3 km, both for a $|\Delta T| > 8$ K, and between 1 and 5 km for a $|\Delta T| < 4$ K. In both cases, IASI detects well the seasonal change in the water isotopic composition with for example the depletion of δD in December–February between the surface and 3 km altitude.

5 Conclusions

This study is a contribution to the WSIBISO project. We have retrieved δD by IASI over land and more specifically over Siberia. The methodology is based on joint $H_2{}^{16}O$ and HDO retrievals, elaborated by Lacour et al. (2012) and using the optimal estimation, for 15 234 retrieved spectra for the year 2011 over YEK.

A different a priori from Lacour et al. (2012) has been used. This a priori information has been built from a set of daily vertical profiles from the isotopic version of LMDZ GCM (LMDZ-iso), representative of the whole year at high latitudes.

IASI has shown its capability to measure the tropospheric δD at two different layers of the atmosphere according to the amplitude of the thermal contrast. IASI is more sensitive in the [0–3 km] altitude range with a high $|\Delta T|$ (e.g. in January) and in the [1–5 km] altitude range with a low $|\Delta T|$ (e.g. in
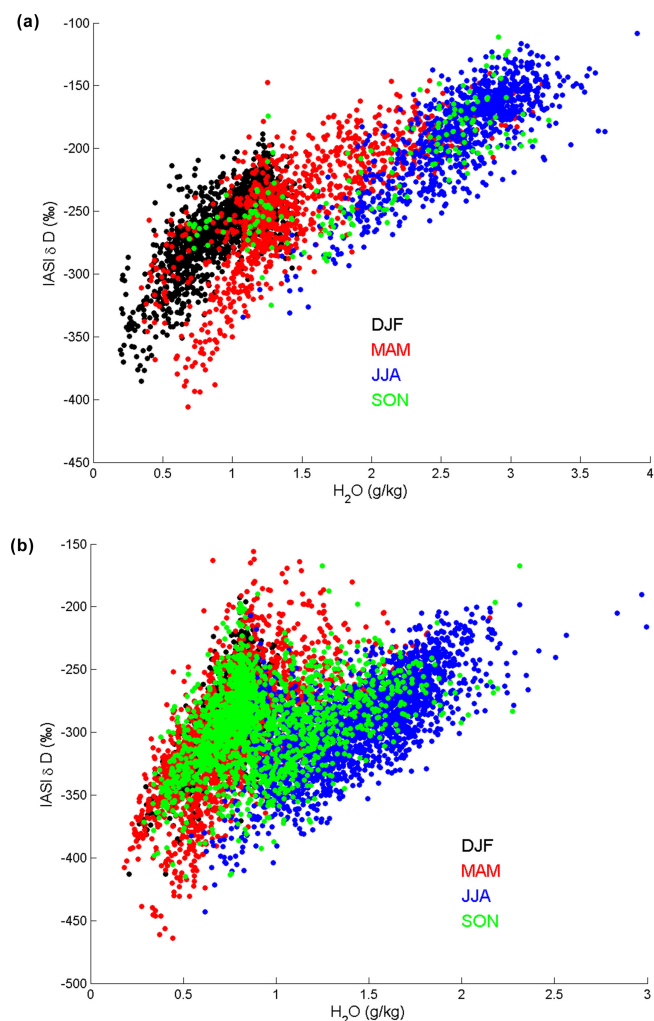
Figure 12. IASI δD as a function of H$_2$O (g kg^{-1}) for the four seasons between 0 and 3 km when $|\Delta T| > 8$ K **(a)** and between 1 and 5 km when $|\Delta T| < 4$ K **(b)**.

July). These layers for which IASI is mostly sensitive complement other δD measurements, performed by other satellite instruments and by ground-based measurements, which are sensitive to δD in different altitude ranges. We show that for the IASI retrievals, the total observational δD errors are lower than 4 % and 7 % close to the surface and in the free troposphere, respectively, with their respective thermal condition.

The data have been evaluated with the simulation from the LMDZ-iso GCM. IASI captures well the seasonal variation for the specific humidity and δD during 2011. IASI and the LMDZ-iso GCM show good agreement on δD following the a posteriori processing of Schneider et al. (2012). We show that IASI is also able to observe the δD day-to-day variability and that the latter compares well with the model simulations ($r \geq 0.6$, up to 0.8 in summer) in both altitude ranges.

References

Boesch, H., Deutscher, N. M., Warneke, T., Byckling, K., Cogan, A. J., Griffith, D. W. T., Notholt, J., Parker, R. J., and Wang, Z.: HDO/H$_2$O ratio retrievals from GOSAT, Atmos. Meas. Tech., 6, 599–612, doi:10.5194/amt-6-599-2013, 2013.

Bony, S. and Emanuel K. A.: A parameterization of the cloudiness associated with cumulus convection: Evaluation using TOGA COARE data, J. Atmos. Sci., 58, 3158–3183, 2001.

Bony, S., Colman, R., Kattsov, V. M., Allan, R. P., Bretherton, C. S., Dufresne, J.-L., Hall, A., Hallegatte, S., Holland, M. M., Ingram, W., Randall, D. A., Soden, B. J., Tselioudis, G., and Webb, M. J.: How well do we understand and evaluate climate change feedback processes?, J. Climate, 19, 3445–3482, 2006.

Bretherton, C. S., Peters, M. E., and Back, L. E.: Relationships between water vapor path and precipitation over the tropical oceans, J. Climate, 17, 1517–1528, 2004.

Clerbaux, C., Boynard, A., Clarisse, L., George, M., Hadji-Lazaro, J., Herbin, H., Hurtmans, D., Pommier, M., Razavi, A., Turquety, S., Wespes, C., and Coheur, P.-F.: Monitoring of atmospheric composition using the thermal infrared IASI/MetOp sounder, Atmos. Chem. Phys., 9, 6041–6054, doi:10.5194/acp-9-6041-2009, 2009.

Craig, H.: Isotopic Variations in Meteoric Waters, Science, 133, 1702–1703, doi:10.1126/science.133.3465.1702, 1961.

Emanuel, K. A.: A scheme for representing cumulus convection in large-scale models, J. Atmos. Sci., 48, 2313–2329, 1991.

Emanuel, K. A. and Zivkovic-Rothman, M.: Development and evaluation of a convection scheme for use in climate models, J. Atmos. Sci., 56, 1766–1782, 1999.

Farquhar, G. D., Cernusak, L. A., and Barnes, B.: Heavy water fractionation during transpiration., Plant Physiol., 143, 11–18, doi:10.1104/pp.106.093278, 2007.

Frankenberg, C., Yoshimura, K., Warneke, T., Aben, I., Butz, A., Deutscher, N., Griffith, D., Hase, F., Notholt, J., Schneider, M., Schrijver, H., and Rockmann, T.: Dynamic Processes Governing Lower-Tropospheric HDO/H$_2$O Ratios as Ob-

served from Space and Ground, Science, 325, 1374–1377, doi:10.1126/science.1173791, 2009.

Frankenberg, C., Wunch, D., Toon, G., Risi, C., Scheepmaker, R., Lee, J.-E., Wennberg, P., and Worden, J.: Water vapor isotopologue retrievals from high-resolution GOSAT shortwave infrared spectra, Atmos. Meas. Tech., 6, 263–274, doi:10.5194/amt-6-263-2013, 2013.

Fueglistaler, S., Dessler, A. E., Dunkerton, T. J., Folkins, I., Fu, Q., and Mote, P. W.: Tropical tropopause layer, Rev. Geophys., 47, RG1004, doi:10.1029/2008RG000267, 2009.

Gat, J. R.: Atmospheric water balance – the isotopic perspective, Hydrol. Process., 14, 1357–1369, doi:10.1002/1099-1085(20000615)14:8<1357::AID-HYP986>3.0.CO;2-7, 2000.

Hartmann, D. L.: Climate Change: Tropical Surprises, Science, 295, 811–812, 2002.

Herbin, H., Hurtmans, D., Turquety, S., Wespes, C., Barret, B., Hadji-Lazaro, J., Clerbaux, C., and Coheur, P.-F.: Global distributions of water vapour isotopologues retrieved from IMG/ADEOS data, Atmos. Chem. Phys., 7, 3957–3968, doi:10.5194/acp-7-3957-2007, 2007.

Herbin, H., Hurtmans, D., Clerbaux, C., Clarisse, L., and Coheur, P.-F.: $H_2^{16}O$ and HDO measurements with IASI/MetOp, Atmos. Chem. Phys., 9, 9433–9447, doi:10.5194/acp-9-9433-2009, 2009.

Hilton, F., Armante, R., August, T., Barnet, C., Bouchard, A., Camy-Peyret, C., Capelle, V., Clarisse, L., Clerbaux, C., Coheur, P.-F., Collard, A., Crevoisier, C., Dufour, G., Edwards, D., Faijan, F., Fourrié, N., Gambacorta, A., Goldberg, M., Guidard, V., Hurtmans, D., Illingworth, S., Jacquinet-Husson, N., Kerzenmacher, T., Klaes, D., Lavanant, L., Masiello, G., Matricardi, M., McNally, A., Newman, S., Pavelin, E., Payan, S., Péquignot, E., Peyridieu, S., Phulpin, T., Remedios, J., Schlüssel, P., Serio, C., Strow, L., Stubenrauch, C., Taylor, J., Tobin, D., Wolf, W., and Zhou, D.: Hyperspectral Earth Observation from IASI: Five Years of Accomplishments, B. Am. Meteor. Soc., 93, 347–370, doi:10.1175/BAMS-D-11-00027.1, 2012.

Hoffmann, G., Werner, M., and Heimann, M.: Water isotope module of the ECHAM atmospheric general circulation model: A study on timescales from days to several years, J. Geophys. Res., 103, 16871–16896, doi:10.1029/98JD00423, 1998.

Hourdin, F. and Armengaud, A.: The use of finite-volume methods for atmospheric advection of trace species. Part I: Test of various formulations in a General Circulation Model, Mon. Weather Rev., 127, 822–837, 1999.

Hourdin, F., Musat, I., Bony, S., Braconnot, P., Codron, F., Dufresne, J.-L., Fairhead, L., Filiberti, M.-A., Friedlingstein, P., Grandpeix, J.-Y., Krinner, G., LeVan, P., Li, Z. X., and Lott, F.: The LMDZ4 general circulation model: Climate performance and sensitivity to parametrized physics with emphasis on tropical convection, Clim. Dynam., 27, 787–813, 2006.

IASI Level 2 Product Guide, EUM/OPS-EPS/MAN/04/0033, v2A, Eumetsat, 12 November 2008.

IPCC: Contribution of Working Groups I, II and III to the Fourth Assessment Report of the Intergovernmental Panel on Climate Change, Core Writing Team, edited by: Pachauri, R. K. and Reisinger, A., Geneva, Switzerland, 104 pp., 2007.

Jouzel, J., Masson-Delmotte, V., Cattani, O., Dreyfus, G., Falourd, S., Hoffmann, G., Minster, B., Nouet, J. , Barnola, J. M., Chappellaz, J., Fischer, H., Gallet, J. C., Johnsen, S., Leuenberger, M.,

Loulergue, L., Luethi, D., Oerter, H., Parrenin, F., Raisbeck, G., Raynaud, D., Schilt, A., Schwander, J., Selmo, E., Souchez, R., Spahni, R., Stauffer, B., Steffensen, J. P., Stenni, B., Stocker, T. F., Tison, J. L., Werner, M., and Wolff, E. W.:: Orbital and millennial Antarctic climate variability over the past 800,000 years, Science, 317, 793–796, 2007.

Kane, D. L.: The impact of hydrologic perturbations on arctic ecosystems induced by climate change, in: Global change and arctic terrestrial ecosystems, edited by: Oechel, W. C., Callahan, T., Gilmanov, T., Holten, J. I., Maxwell, B., Molau, U. and Sveinbjörnsson, B., Springer-Verlag New York, Inc., 63–81, 1997.

Kiehl, J. T. and Trenberth, K. E.: Earth's Annual Global Mean Energy Budget, Bull. Amer. Meteor. Soc., 78, 197–208, doi:10.1175/1520-0477(1997)078<0197:EAGMEB>2.0.CO;2, 1997.

Lacour, J.-L., Risi, C., Clarisse, L., Bony, S., Hurtmans, D., Clerbaux, C., and Coheur, P.-F.: Mid-tropospheric δD observations from IASI/MetOp at high spatial and temporal resolution, Atmos. Chem. Phys., 12, 10817–10832, doi:10.5194/acp-12-10817-2012, 2012.

Lapshina, E. D., Velichko, A. A., Borisova, O. K., Kremenettsky, K. V., and Pologova, N. N.: Holocene dynamics of peat accumulation In: Bleuten W & Lapshina ED, (EDS) Carbon Storage and Atmospheric Exchange by west Siberian Peatlands, FGUU Scientific Reports 2001-1, Utrecht,(NL), ISBN 90- 806594-1-X 47–72, 2001.

Lee, J.-E., Fung, I., DePaolo, D., and Fennig, C. C.: Analysis of the global distribution of water isotopes using the NCAR atmospheric general circulation model, J. Geophys. Res., 112, D16306, doi:10.1029/2006JD007657, 2007.

Luo, Z. and Rossow, W. B.: Characterizing tropical cirrus life cycle, evolution, and interaction with upper-tropospheric water vapor using Lagrangian trajectory analysis of satellite observations, J. Climate, 17, 4541–4563, 2004.

Nassar, R., Bernath, P. F., Boone, C. D., Gettelman, A., McLeod, S. D., and Rinsland, C. P.: Variability in HDO/H_2O abundance ratios in the tropical tropopause layer, J. Geophys. Res., 112, 1–11, doi:10.1029/2007JD008417, 2007.

Pougatchev, N., August, T., Calbet, X., Hultberg, T., Oduleye, O., Schlüssel, P., Stiller, B., Germain, K. St., and Bingham, G.: IASI temperature and water vapor retrievals – error assessment and validation, Atmos. Chem. Phys., 9, 6453–6458, doi:10.5194/acp-9-6453-2009, 2009.

Risi, C., Bony, S., Vimeux, F., and Jouzel, J.: Water stable isotopes in the LMDZ4 General Circulation Model: Model evaluation for present day and past climates and applications to climatic interpretation of tropical isotopic records, J. Geophys. Res., 115, D12118, doi:10.1029/2009JD013255, 2010.

Risi, C., Noone, D., Worden, J., Frankenberg, C., Stiller, G., Kiefer, M., Funke, B., Walker, K., Bernath, P., Schneider, M., Wunch, D., Sherlock, V., Deutscher, N., Griffith, D., Wennberg, P. O., Strong, K., Smale, D., Mahieu, E., Barthlott, S., Hase, F., García, O., Notholt, J., Warneke, T., Toon, G., Sayres, D., Bony, S., Lee, J., Brown, D., Uemura, R., and Sturm, C: Process-evaluation of tropospheric humidity simulated by general circulation models using water vapor isotopologues: 1. Comparison between models and observations, J. Geophys. Res., 117, D05303, doi:10.1029/2011JD016621, 2012a.

Risi, C., Noone, D., Worden, J., Frankenberg, C., Stiller, G., Kiefer, M., Funke, B., Walker, K., Bernath, P., Schneider, M., Bony, S., Lee, J., Brown, D., and Sturm, C.: Process-evaluation of tropospheric humidity simulated by general circulation models using water vapor isotopic observations: 2. Using isotopic diagnostics to understand the mid and upper tropospheric moist bias in the tropics and subtropics, J. Geophys. Res., 117, D05304, doi:10.1029/2011JD016623, 2012b.

Risi, C., Noone, D., Frankenberg, C., and Worden, J.: Role of continental recycling in intraseasonal variations of continental moisture as deduced from model simulations and water vapor isotopic measurements, Water Resour. Res., 49, 4136–4156, doi:10.1002/wrcr.20312, 2013.

Rodgers, C. D.: Inverse methods for atmospheric sounding: theory and practise, World Scientific, 2000.

Rothman, L. S., Gordon, I. E., Barbe, A., Benner, D. C., Bernath, P. F., Birk, M., Boudon, V., Brown, L. R., Campargue, A., Champion, J., Chance, K., Coudert, L. H., Dana, V., Devi, V. M., Fally, S., Flaud, J., Gamache, R. R., Goldman, A., Jacquemart, D., Kleiner, I., Lacome, N., Lafferty, W. J., Mandin, J., Massie, S. T., Mikhailenko, S. N., Miller, C. E., Moazzen-Ahmadi, N., Naumenko, O. V., Nikitin, A. V., Orphal, J., Perevalov, V. I., Perrin, A., Predoi-Cross, A., Rinsland, C. P., Rotger, M., Simeckova, M., Smith, M. A. H., Sung, K., Tashkun, S. A., Tennyson, J., Toth, R. A., Vandaele, A. C., and Vander Auwera, J.: The HITRAN 2008 molecular spectroscopic database, J. Quant. Spectrosc. Radiat. Transfer, 110, 533–572, doi:10.1016/j.jqsrt.2009.02.013, 2009.

Schmidt, G. A., Ruedy, R. A., Miller, R. L., and Lacis, A. A.: Attribution of the present-day total greenhouse effect, J. Geophys. Res., 115, D20106, doi:10.1029/2010JD014287, 2010.

Schneider, M. and Hase, F.: Optimal estimation of tropospheric H_2O and ΔD with IASI/METOP, Atmos. Chem. Phys., 11, 11207–11220, doi:10.5194/acp-11-11207-2011, 2011.

Schneider, M., Hase, F., and Blumenstock, T.: Ground-based remote sensing of HDO/H_2O ratio profiles: introduction and validation of an innovative retrieval approach, Atmos. Chem. Phys., 6, 4705–4722, doi:10.5194/acp-6-4705-2006, 2006.

Schneider, M., Yoshimura, K., Hase, F., and Blumenstock, T.: The ground-based FTIR network's potential for investigating the atmospheric water cycle, Atmos. Chem. Phys., 10, 3427–3442, doi:10.5194/acp-10-3427-2010, 2010.

Schneider, M., Barthlott, S., Hase, F., González, Y., Yoshimura, K., García, O. E., Sepúlveda, E., Gomez-Pelaez, A., Gisi, M., Kohlhepp, R., Dohe, S., Blumenstock, T., Wiegele, A., Christner, E., Strong, K., Weaver, D., Palm, M., Deutscher, N. M., Warneke, T., Notholt, J., Lejeune, B., Demoulin, P., Jones, N., Griffith, D. W. T., Smale, D., and Robinson, J.: Ground-based remote sensing of tropospheric water vapour isotopologues within the project MUSICA, Atmos. Meas. Tech., 5, 3007–3027, doi:10.5194/amt-5-3007-2012, 2012.

Sherwood, S. C., Ingram, W., Tsushima, Y., Satoh, M., Roberts, M., Vidale, P. L., and O'Gorman, P. A.: Relative humidity changes in a warmer climate, J. Geophys. Res., 115, D09104, doi:10.1029/2009JD012585, 2010.

Soden, B. J. and Held, I. M.: An assessment of climate feedbacks in coupled ocean-atmosphere models, J. Climate, 19, 3354–3360, doi:10.1175/JCLI3799.1, 2006.

Van Leer, B.: Towards the ultimate conservative difference scheme: IV. A new approach to numerical convection, J. Comput. Phys., 23, 276–299, 1977.

Wiegele, A., Schneider, M., Hase, F., Barthlott, S., García, O. E., Sepúlveda, E., González, Y., Blumenstock, T., Raffalski, U., Gisi, M., and Kohlhepp, R.: The MUSICA MetOp/IASI H_2O and ΔD products: characterisation and long-term comparison to NDACC/FTIR data, Atmos. Meas. Tech. Discuss., 7, 3915–3952, doi:10.5194/amtd-7-3915-2014, 2014.

Worden, J., Bowman, K., Noone, D., Beer, R., Clough, S., Eldering, A., Fisher, B., Goldman, A., Gunson, M., Herman, R., Kulawik, S. S., Lampel, M., Luo, M., Osterman, G., Rinsland, C., Rodgers, C., Sander, S., Shephard, M., and Worden, H.: Tropospheric emission spectrometer observations of the tropospheric HDO/H_2O ratio: estimation approach and characterization, J. Geophys. Res.-Atmos., 111, D16309, doi:10.1029/2005jd006606, 2006.

Worden, J., Noone, D., and Bowman, K.: Importance of rain evaporation and continental convection in the tropical water cycle, Nature, 445, 528–532, doi:10.1038/nature05508, 2007.

Worden, J., Kulawik, S., Frankenberg, C., Payne, V., Bowman, K., Cady-Peirara, K., Wecht, K., Lee, J.-E., and Noone, D.: Profiles of CH_4, HDO, H_2O, and N_2O with improved lower tropospheric vertical resolution from Aura TES radiances, Atmos. Meas. Tech., 5, 397–411, doi:10.5194/amt-5-397-2012, 2012.

Zakharov, V. I., Imasu, R., Gribanov, K. G., Hoffmann G., and Jouzel, J.: Latitudinal Distribution of Deuterium Ratio in the Atmospheric Water Vapor Retrieved from IMG/ADEOS Data, Geophys. Res. Lett., 31, L12104, doi:10.1029/2004GL019433, 2004.